# Hidden Local Symmetry Breaking in Silver Diamondoid Compounds is Root Cause of Ultralow Thermal Conductivity

Hongyao Xie, Emil S. Bozin, Zhi Li, Milinda Abeykoon, Soham Banerjee, James P. Male, G. Jeffrey Snyder, Christopher Wolverton, Simon J. L. Billinge, and Mercouri G. Kanatzidis

Dr. Hongyao Xie, Prof. Mercouri G. Kanatzidis
*Department of Chemistry, Northwestern University, Evanston, Illinois 60208, USA.*
Email: m-kanatzidis@northwestern.edu.

Dr. Emil S. Bozin, Prof. Simon J. L. Billinge
*Condensed Matter Physics and Materials Science Division, Brookhaven National Laboratory, Upton, New York 11973, USA*

Dr. Zhi Li, Dr. James P. Male, Prof. G. Jeffrey Snyder, Prof. Christopher Wolverton,
*Department of Materials Science and Engineering, Northwestern University, Evanston, Illinois 60208, USA.*

Dr. Milinda Abeykoon,
*Photon Sciences Division, Brookhaven National Laboratory, Upton, New York 11973, USA*

Dr. Soham Banerjee,
*Deutsches Elektronen-Synchrotron DESY, Notkestrasse 85, 22607 Hamburg, Germany*

Prof. Simon J. L. Billinge
*Department of Applied Physics and Applied Mathematics, Columbia University, New York, New York 10027, USA*

Keywords: chalcopyrites, emphanisis, thermal conductivity, thermoelectrics

**Abstract:**

Typically, conventional structure transitions occur from a low symmetric state to a higher symmetry state upon warming. Here, we report an unexpected local symmetry breaking in the tetragonal diamondoid compound $AgGaTe_2$, which upon warming evolves continuously from an undistorted ground state to a locally distorted state while retaining average crystallographic symmetry. This distorted state, caused by the weak $sd^3$ orbital hybridization of tetrahedral Ag atoms, causes their displacement off the tetrahedron center and promotes a global distortion of the crystal structure resulting in strong acoustic–optical phonon scattering and an ultralow lattice thermal conductivity of 0.26 W $m^{-1}$ $K^{-1}$ at 850 K in $AgGaTe_2$. Our findings explain the underlying reason for the unexpectedly low thermal conductivities of silver-based compounds compared to copper-based analogs and provide a guideline to suppressing heat transport in diamondoid and other materials.

**Main Text:**

The major crystallographic architecture that has dominated the field of thermoelectrics is the rocksalt structure. A substantial majority of advanced thermoelectric materials belong to this structure type or a variant. For example, PbQ,[1-3] SnQ (Q=S, Se, Te),[4-6] and even the two-dimensional $Bi_2Te_3$ structure[7] fall within this motif, the latter being an ordered vacancy variant. The half-Heusler compounds[8] are a stuffed form. The diamond structure motif, however, historically has been avoided in thermoelectric materials research despite the generally high carrier mobilities it favors, because such tetrahedral structures are more tightly packed and usually have stiffer lattices than the rocksalt materials. They present high phonon frequencies and velocities giving rise to very high thermal conductivity.[9, 10] Typical compound semiconductors in this class include the zincblende-, wurtzite- and the chalcopyrite-type materials.[11-14] The $AMQ_2$ (A = Cu, Ag; M = Al, Ga, In, Tl; Q = S, Se, Te) ternary diamondoid compounds are a large family of relatively wide band gap ($E_g$ > 1 eV) semiconductors that possess various unique transport properties, and have many important applications in photovoltaic cells,[15] nonlinear optics,[16] and thermoelectricity.[11, 13] Recently, a thermoelectric figure of merit (*ZT*) beyond 1.6 has been reported in $Cu_{1-x}Ag_xInTe_2$[17] and $(Cu_{1-x}Ag_x)(In_{1-y}Ga_y)Te_2$ diamondoid compounds[18, 19]. These performance advances have drawn intense interest in fundamental understanding of the electronic and heat transport properties of the diamondoid compounds in greater detail.

The ternary diamondoid compounds (chalcopyrites) derived from the diamond structure can be considered as a double sphalerite cell (M'Q) stacked along the c-axis, where the divalent M' cation is replaced by monovalent A and trivalent M, see **Fig. 1a**.

Among compositions with the identical crystal structure, the Ag-based diamondoid compounds exhibit a much lower intrinsic lattice thermal conductivity than the Cu-based materials.[20-22] Although it is expected that a composition with heavier atoms (e.g. Ag vs Cu) will have lower thermal conductivity, in this particular case the difference is much larger than predicted from the classical theoretical physics concepts. A simple equation was proposed by Keyes[23] to express the role of mass and crystal volume in the thermal conductivity:

$$\kappa T = \beta \frac{T_m^{3/2}}{m_a^{1/2} V_a^{2/3}} \quad (1)$$

where $\kappa$ is the thermal conductivity, $T$ is the temperature, $\beta$ is the structural parameter that depends on Grüneisen parameter and Lindemann criterion limit, $T_m$ is the melting point of the crystal, $m_a$ is the mean atomic weight and $V_a$ is the volume per gram atom. From this relationship it would be intuitive to attribute the low thermal conductivity of Ag-based diamondoid compounds to the large atomic mass and volume of Ag. **Fig. 1b** shows the relationship between room temperature lattice thermal conductivities and the weight factor: $T_m^{3/2} m_a^{-1/2} V_a^{-2/3}$ for different diamondoid materials.[24-31] Obviously, the Cu-based compounds show a much stronger mass and volume dependence behavior than that of the Ag-based materials, which lead to a 5 fold larger $\beta$ factor in the former. According to Keyes' model, the weight factor fails to explain the large disparity in heat transport properties between these materials, and the fundamental reason should be attributed to the factor of 5 difference in structural parameter, $\beta$. Although in most of the cases, the $\beta$ factor is considered as a constant for a group of variants, here, the greatly disparate $\beta$ factors can

only be explained by the appreciably different anharmonicity between Cu- and Ag-based diamondoid materials.

$AgGaTe_2$, $CuGaTe_2$ and $CuInTe_2$ are excellent candidates to study this disparity in diamondoid materials. As shown in **table. S1**, the crystal volumes and molecular weights of $AgGaTe_2$ and $CuInTe_2$ are almost identical. However, the $AgGaTe_2$ shows a much lower lattice thermal conductivity (**Fig. 1c**), which sits at 1.65 W $m^{-1}$ $K^{-1}$ at room temperature and decreases to the ultralow value of 0.26 W $m^{-1}$ $K^{-1}$ at 850 K, less than 1/3 of $CuInTe_2$ in the entire temperature region. Therefore, the influence of mass and volume on the thermal conductivity is the same for $AgGaTe_2$ and $CuInTe_2$. More importantly, the difference in Grüneisen parameter (anharmonicity) of these compounds is only ~7%, and the difference of their sound velocity is also only ~8% (**table. S1**), all of this is insufficient to account for the observed difference in the lattice thermal conductivity. How then does the large discrepancy in heat conductivity arise between these two materials? Clearly, the conventional heat transport model is inadequate to explain this issue, and the understanding of the underlying mechanisms of the extremely low thermal conductivity of Ag-based diamondoid compounds remains incomplete.

When we look back to the known crystallographic data, a large tetragonal distortion parameter ($\eta$ =|2-c/a| ; c and a are the length of c-axis and a-axis, respectively)[32] exists in $AgGaTe_2$, which is ~28 times larger than that of the $CuInTe_2$ (**table. S1**). We note that this tetragonal crystallographic distortion is in regard to the cubic symmetry of the parent ZnS structure type from which it derives and should not be confused with a local symmetry-breaking distortion associated with the silver atoms. As we will show, the latter is randomly oriented and on average does not reduce that tetragonal symmetry, which is not a typical

phase transition. A larger $\eta$ implies the chalcopyrite lattice exhibits a large distortion from the ideal diamond structure. Intuitively one might think of this as the key to explain the large discrepancy in heat conductivity. The relationship between $\eta$ and thermal conductivity for different diamondoid compounds is plotted in **Fig. 1d**. Here the ordinate is the thermal conductivity multiplied by crystal volume ($V$) and formula weight ($m$), and the data follow the empirical relationship $\kappa \cdot T \sim (1/m \cdot V) \cdot (1/\eta)$ as shown by the dashed line. It is apparent from this figure that all Ag compounds have high lattice distortion parameters and much lower thermal conductivities compared to the Cu analogs, which strongly supports the connection between the large crystallographic distortion and low thermal conductivity in Ag-based diamondoid compounds. Thus, the question is, what is the underlying cause of the high crystallographic distortion $\eta$ for Ag compounds and how does it affect the thermal conductivity of diamondoid compounds? This is not only a core topic of high scientific interest, but also important in future applications of diamondoid materials.

In this study, we investigate the impact of lattice dynamics on the thermal transport properties of $AgGaTe_2$, $CuGaTe_2$ and $CuInTe_2$ *via* synchrotron X-ray atomic pair distribution function (PDF) analysis and first principles theoretical calculations. We discovered a local broken symmetry on the Ag site of $AgGaTe_2$, which emerges continuously upon warming from an undistorted ground state to a local distorted state, in contrast to conventional structure transitions in which distortions emerge upon cooling. The directions of the local distortions of the Ag sites are random on the short-range therefore the average crystallographic symmetry is retained. This type of local distortion has its origins in the peculiar relativistic effects on the electronic structure of Ag and their impact on the tetrahedral bonding. The distortion increases continuously on warming and

is promoted by entropy. This is therefore is not a standard phase transition and has been referred to as *emphanisis*.[33, 34] The local distortion of Ag introduces a few extremely low frequency optical phonons at ~20 $cm^{-1}$, resulting in a strong acoustic–optical phonon scattering and an ultralow thermal conductivity of 0.26 W $m^{-1}$ $K^{-1}$ at 850 K in $AgGaTe_2$. Our theoretical analysis suggests a large difference in energy between the s and d electron orbitals of the Ag leads to the weak $sd^3$ orbital hybridization, which is the driving force of the local distortion of Ag. This local distortion was evidenced by X-ray PDF analysis and is in fact off-centering displacements of Ag atoms away from the tetrahedral center which increase on warming. This drives the global crystal structure distortion as measured by the tetragonal distortion parameter $\eta$. This is the first example of emphanisis being observed in a tetrahedral diamondoid compound. It has been believed that the emphanisis phenomenon occurs only through the actions of the $ns^2$ lone pair of electrons associated with main-group metals and octahedral coordination environments such as $Sn^{2+}$, $Pb^{2+}$ and $Sb^{3+}$, and has been observed in PbQ, SnQ (Q= S, Se, Te), rock-salt $AgSbSe_2$ and cubic halide perovskites ($CsSnBr_3$).[33, 35-37] Significantly, in diamondoid systems reported here the mechanism does not involve $ns^2$ lone pairs, demonstrating that this phenomenon is more diverse than previously thought. Our findings expose the chimeric nature of Ag in these materials. They demonstrate the weak Ag orbital hybridization can induce the emphanisis effect and strongly impact the thermal conductivity of diamondoid compounds. They also establish a link between $\eta$ and thermal conductivity in these materials.

**The local interatomic structure in $AgGaTe_2$ and $CuGaTe_2$**

The structure of $AgGaTe_2$ on different length-scales was assessed in the high

temperature regime by synchrotron PDF analysis, using $CuGaTe_2$ as a reference. The PDF is based on a Fourier transform of appropriately collected, corrected, and reduced total scattering data, providing a distribution of interatomic distances in a material[38], and is a powerful probe for nanoscale structure investigations[39]. Two sets of PDF measurements were carried out under slightly different experimental conditions, referred to as *exp1* (higher r-resolution, narrower T-range) and *exp2* (lower r-resolution, broader T-range) (see Supplementary Materials for details). The PDF data of $AgGaTe_2$ on length-scales > 1 nm and $CuGaTe_2$ (on all length-scales) are in excellent agreement with the tetragonal crystallographic model[40] at all temperatures, **Fig. 2a**. However, comparison of the tetragonal lattice parameters reveals an unusual difference in the temperature evolution between the two systems: while both *a*- and *c*- $CuGaTe_2$ parameters increase on warming as expected, the *c*-parameter of $AgGaTe_2$ displays pronounced and robust negative thermal expansion, **Fig. 2b**, and therefore a strong enhancement in $\eta$ with temperature.

The anomalous behavior of $AgGaTe_2$ is further underscored by the unphysically enlarged isotropic atomic displacement parameters (ADP) of Ag and Te, as compared to ADPs of Cu and Te in $CuGaTe_2$, **Fig. 2c**. Releasing symmetry allowed anisotropies of the ADPs for the Ag site results in larger yet values for the $U_{11}/U_{22}$ in the *ab*-plane and a smaller $U_{33}$ along the tetragonal axis. This behavior is indicative of disorder in the Ag positions within the planes containing Ag and Ga, **Fig. 2e**, as well as on the Te sublattice. A closer look at the crystallographic global model fit to the PDF, **Fig. 2a**, reveals its failure on the sub-nanometer scale, with observable signature of local distortions spanning ~8 Å in the differential PDF, $\Delta G(r)$. The S-shaped misfit under the nearest neighbor (NN) PDF peak at around 2.5 Å, **Fig. 2f** (top), is indicative of a displacive distortion. The misfits of the

subsequent PDF peaks are consistent with distortions of the Te-Te distances. Concerning the NN peak, one more difference between the $CuGaTe_2$ and $AgGaTe_2$ behavior can be established in a model-independent way when data at two extreme temperatures of our high-resolution measurements are compared, **Fig. 2d**. The differential PDF established between the 320 K and 485 K $CuGaTe_2$ data (top panel) is largely symmetric with respect to the feature centroid, whereas the corresponding feature in $AgGaTe_2$ data (bottom panel) exhibits an observable asymmetry with more intensity in the part of the differential to the right of the centroid. If related to the underlying distortion, this would imply its increased strength on warming consistent with emphanisis. To explore this, we considered several simple broken symmetry models to fit the PDF data in the range below $r < 8.5$ Å (see Supplementary Materials for details). The most prominent model, sketched in **Fig. 2e** (middle, right), involves Ag displacements along <100> and <010> directions, marked by gray arrows, where Ag displaces towards one of the four Te-Te edges within the $Te_4$ tetrahedral unit. Due to the close packing of the structure, the Te atoms in that model were allowed to displace away in response, roughly along the $Te_4$ edge direction, as indicated by the purple arrows. In the model, the ADPs were set to values from reference $CuGaTe_2$ and kept fixed. This resulted in a significantly improved fit over the $r < 8.5$ Å range of the PDF, **Fig. 2f** (bottom).

To account for Ag appearing undisplaced on average in the global structure, in this model the displacements of the NN Ag in the neighboring planes were set to alternate between <100> and <010> directions, **Fig. 2e** (right). Large amplitude Ag and Te displacements were refined, and their temperature evolution is shown in **Fig. 2g**. These trends appear linear and can be extrapolated to lower temperature, as depicted by dotted

lines, suggesting that the local distortion increases continuously on warming. This emphanitic behavior is strikingly similar to the off-centering of Pb and Sn observed in binary lead and tin chalcogenides, where the state of broken local symmetry appears and evolves out of a globally symmetric ground state upon warming[33, 35]. The observed misfit of the global model over~8 Å implies that the displacements of the NN Ag are correlated over this length-scale, as incorporated in the model. Notably, the Ag-Te-Ag angle between the neighboring $AgTe_4$ units, marked θ in **Fig. 2e** (right), decreases upon warming, **Fig. 2f**, suggesting that the observed negative thermal expansion in the $AgGaTe_2$ *c*-lattice parameter is not only a likely consequence of the rotations of tetrahedral structural units invoked by local Ag off-centering, but that it could be considered as its macroscopic signature. Although total scattering-based PDF does not discriminate between inelastic and elastic scattering and thereby probes the instantaneous atomic structure, this local state is expected to be fluctuating, where the zero net displacement is obtained through statistical averaging of different available distortion directions indicated by dashed arrows in **Fig. 2e** (middle).

**Ultralow thermal conductivity of $AgGaTe_2$**

The PDF analysis showed dramatic difference in local structure between $AgGaTe_2$ and $CuGaTe_2$, which increases monotonically with rising temperature and should account for the large discrepancy in thermal conductivity of these materials. To understand the correlation between local emphanitic Ag off-centering (symmetry breaking upon warming) and the ultralow thermal conductivity of $AgGaTe_2$, we performed density functional theory (DFT) calculations to obtain the phonon dispersions and phonon density of states for

$AgGaTe_2$, $CuGaTe_2$ and $CuInTe_2$, see **Fig. 3a and fig. S7**. As expected, $AgGaTe_2$ possesses the lowest Debye frequency (the highest frequency of the acoustic phonons), which is ~ 25-30 $cm^{-1}$, and is only about half of that (~ 50 $cm^{-1}$) for $CuGaTe_2$ and $CuInTe_2$. The low Debye frequency is consistent with the lower phonon velocity of $AgGaTe_2$, **table S1**.

Moreover, a number of low frequency optical modes exist around the Debye frequency for all these materials, but in $AgGaTe_2$ exclusively, a few extremely low frequency optical phonons emerge at the Γ point with a frequency of ~20 $cm^{-1}$ – a lower value than the compound's Debye frequency, see the pink regions in **Fig. 3a**. The projected phonon density of states suggests these extremely low frequency optical phonons stem from the Ag and Te atoms. Two optical modes with lowest frequency are marked as optical mode #1 and mode #2 in **Fig. 3a**, and we visualize the atomic vibrations around the Γ point of these optical modes, see **Fig. 3b and 3c** (here the red arrows indicate the moving direction of atom). This clearly shows that Ag has a large movement from its equilibrium position and that the intense vibration of Ag pushes the Te atoms distorting the Te-tetrahedron, which in turn produces the extremely low frequency optical phonons in $AgGaTe_2$. This result is consistent with the PDF analysis and demonstrates that the local Ag off-centering is responsible for the extremely low frequency optical phonons. Furthermore, an avoided crossing occurs in the same regions between the acoustic phonons and the low-frequency optical phonons (**Fig. 3a**), suggesting strong coupling between the acoustic and optical phonons in $AgGaTe_2$. This phonon-phonon coupling behavior has been observed in other Ag-based diamondoid compounds, such as $AgInTe_2$[17], $AgInSe_2$[22] and $AgGaSe_2$[41] which also possess ultralow thermal conductivity thus implicating the emphanitic effects in these systems as well.

This acoustic-optical phonon coupling introduces strong phonon scattering and increases the scattering rate, thus suppressing the heat conductivity in a material.[10, 42] The frequency dependent phonon scattering rates of $AgGaTe_2$, $CuGaTe_2$ and $CuInTe_2$ are shown in **Fig. 3d and fig. S8**. Generally, the phonon scattering rate increases with increasing phonon frequency (energy), just as seen in $CuGaTe_2$ and $CuInTe_2$, **fig. S8**. Here we are only concerned with acoustic phonons (red circles), since they are the major heat carrying phonons. However, for $AgGaTe_2$, the acoustic phonon scattering rate shows unusually high values at 20 to 35 $cm^{-1}$, and then anomalously drops with increasing phonon frequency, see **Fig. 3d**. The optical phonons also exhibit anomalously large scattering rate at the frequency of 20 to 35 $cm^{-1}$. Considering the frequency overlap between acoustic and optical phonons in $AgGaTe_2$, and the anomalous increase in phonon scattering rate in the overlapping region (20 to 35 $cm^{-1}$), the hybridized acoustic-optical phonons with frequency of 20 to 35 $cm^{-1}$ are expected to be intensely scattered. The average acoustic phonon scattering rate of $AgGaTe_2$ is 0.1231 THz, substantially higher than the corresponding value of $CuInTe_2$ (0.0269 THz) and $CuGaTe_2$ (0.0329 THz). These results reveal that the local Ag off-centering introduces major acoustic-optical phonon scattering in $AgGaTe_2$.

The phonon-phonon coupling can be experimentally probed by the low temperature heat capacity[43, 44] and analyzed using the Debye-Einstein model[43, 45]. **Fig. 3e** shows the plot of low temperature heat capacity data as $C_p/T^3$ versus $T$ in the temperature range from 2 to 40 K, which clearly displays a pronounced maximum of $C_p/T^3$ around 10 K. This peak is referred to as the Boson peak,[46, 47] and has been observed in other intrinsic low thermal conductivity non-diamondoid materials, such as $CsSnBr_3$,[42] and $TlInTe_2$[44]. The Boson peak is regarded as a sign of the coupling between low-frequency optical phonons and

acoustic phonons and is ascribed to the presence of additional vibrational states in the lattice. As shown in **Fig. 3e**, the simple Debye model fails to explain the low temperature heat capacity of $AgGaTe_2$, indicating that the acoustic phonon modes alone are insufficient to account for the observed heat capacity. However, the experimental data can be well described by introducing two Einstein oscillators in the Debye host, see **Fig. 3e and fig. S13**, which further corroborates the contribution of acoustic-optical phonon coupling in $AgGaTe_2$.

To further assess the strength of phonon scattering and the role of acoustic-optical phonon coupling in the lattice thermal conductivity of $AgGaTe_2$, we employed the Debye–Callaway model[8, 48-51]. We first calculated the spectral lattice thermal conductivity $\kappa(\omega)$ of $AgGaTe_2$, which reflects the impact of different scattering mechanisms on the thermal conductivity at different phonon frequencies, see **Fig. 3f**. The Umklapp scattering, grain boundary scattering, point defect scattering, and acoustic–optical phonon scattering,[52] have all been considered as the important scattering mechanisms. Obviously, the acoustic–optical phonon scattering involves the intermediate frequency phonons and is important for pushing the low lattice thermal conductivity of $AgGaTe_2$ to extremely low values. A local minimum of $\kappa(\omega)$ is observed at ~ 28 $cm^{-1}$, indicating phonons with frequencies close to this value are intensely scattered, thus, inefficient to conduct the heat. This result agrees with the DFT-calculated phonon scattering rate contributed by the acoustic–optical phonon scattering (**Fig. 3d**). The contribution of different scattering processes to the lattice thermal conductivity of $AgGaTe_2$ is shown in **Fig. 3g**, and indicates acoustic–optical phonon scattering can reduce the lattice thermal conductivity of $AgGaTe_2$ by 64% at 850 K.

**Electronic origin of Ag off-centering and impact on the global tetragonal crystallographic distortion**

Although the above discussion confirms that the ultralow thermal conductivity of $AgGaTe_2$ is derived from its local symmetry being continuously broken upon warming (local Ag tetrahedral off-centering), it does not address the underlying driving force behind it. To explore the chemical bonding state and further understand the electronic bonding effects, we performed DFT-calculations and assessed the crystal orbital Hamiltonian populations (COHP) and the interatomic force constants of $AgGaTe_2$, $CuGaTe_2$ and $CuInTe_2$, see **fig. S14 and fig. S15**. The integrated COHP of Ag has smaller absolute values than Cu, Ga and In, and agrees with the interatomic force constant data (**fig. S15**) indicating the weaker chemical bonding of Ag-Te in the diamondoid structure.

The COHP in **Fig. 4a-c** more transparently shows the contributions of different electronic orbitals to the bonding state. The s–p and d–p interactions between the transition metals (s-orbitals and d-orbitals) and anions (p-orbitals) dominate the valence band energies and the chemical bonding in both Ag and Cu compounds. Notably, the energies of anti-bonding states deriving from d–p interactions (the red curve) in Ag-Te bonding are much lower than for the Cu-Te bonds. This low 4d-5p anti-bonding state destabilizes and weakens the Ag-Te bonds. The origin of this weak Ag-Te bond is illuminated by the schematic molecular orbital diagram of Cu-Te and Ag-Te, **Fig. 4d**. The energy of Ag d-orbitals is much lower than that of Cu[53]. This results in a lower (by ~1 eV) 4d-5p anti-bonding state in the Ag-Te bond and makes its energy closer to the 5s-5p bonding state, thus weakening it.

More importantly, within the valence-bond (VB) theory framework, the geometries

of transition metal ions have been rationalized through the use of the $sd^n$ hybridization model.[54, 55] According to this theory, in the $AMQ_2$ diamondoid compounds, the Ag and Cu should adopt the $sd^3$ hybridization to establish a perfect tetrahedral coordination geometry.[54] Since atomic orbitals with similar energy can hybridize to a greater degree, higher energy differences between the interacting orbitals would lead to a lower level of hybridization. In group-11 elements as one moves from Cu to Ag and Au, the influence of relativistic effects as it affects the s-d hybridization is in the anomalous order of Ag < Cu < Au.[56] Thus, the largest energy difference between the 5s and 4d electronic orbitals occurs in Ag and this should result in weaker $sd^3$ hybridization, making it amenable to deviations from tetrahedral geometry. This is the origin of the local off-centering Ag distortion, in contrast to Cu where such predispositions are much less pronounced. Besides, the strength of bonding interaction is mainly determined by the orbital overlap. Therefore, the tetrahedral off-centering distortion implies a smaller orbital overlap. Furthermore, the off-centering behavior results in negative c-axis thermal expansion, which in turn leads to a larger tetragonal crystallographic distortion value ($\eta$), **Fig. 4e**. Thus, the A-Q bonding strength which derives from weaker $sd^3$ hybridization and causes off-centering, the crystallographic distortion parameter ($\eta$) and the thermal conductivity of the diamondoid structure are closely linked, resulting in relationship shown in **Fig. 1d**.

Finally, we performed a theoretical experiment to expose the connection between thermal conductivity and crystallographic distortion. **Fig. 4f** depicts the DFT-calculated thermal conductivities of $AgGaTe_2$, $CuGaTe_2$, and a hypothetical test model. The DFT calculation reproduces an extremely low thermal conductivity in $AgGaTe_2$ as well as a high value in $CuGaTe_2$, consistent with the experimental results. The test model corresponds to

a hypothetical situation in which the $CuGaTe_2$ chemistry is retained but is enforced to adopt the lattice parameters of $AgGaTe_2$, and the atoms are allowed to relax to their equilibrium positions. By implanting the ideal $CuGaTe_2$ ($\eta$=0.0172) into the distorted $AgGaTe_2$ lattice ($\eta$ =0.1037), the calculation also returns a very low thermal conductivity in this hypothetical structure. The fundamental reason of this low thermal conductivity is the weakening of Cu-Te bonding imposed by the hypothetical distortion. Therefore, the higher crystallographic distortion ($\eta$) is a macroscopic signature of local atom displacements and a harbinger of a lower thermal conductivity in diamondoid structures.

In conclusion, the local structure of Ag in chalcopyrite is chimeric. The perfect tetrahedral geometry in reality an average of off-centering distortions occurring in a dynamic fashion. The unusual local symmetry breaking in $AgGaTe_2$, is enhanced upon warming. This emphanitic local distortion of the Ag coordination has remained hidden despite the long history of chalcopyrite materials. It is electronic in origin, deriving from the relativistic idiosyncrasies of Ag, which results in weakened $sd^3$ orbital hybridization. This drives Ag off its tetrahedral center and results in strong acoustic–optical phonon scattering and an ultralow thermal conductivity of 0.26 W $m^{-1}$ $K^{-1}$ at 850 K in $AgGaTe_2$. This local off-centering of Ag atoms explains the negative c-axis thermal expansion and triggers the well-known tetragonal distortion of the crystal structure. Our work validates the simple relationship $\kappa \cdot T \sim (1/m \cdot V) \cdot (1/\eta)$ to predict the thermal conductivity of the diamondoid materials. Similar electronic phenomena associated with weakened $sd^3$ orbital hybridization maybe anticipated in Hg-containing II-VI variants. Our findings provide a new guideline to designing systems with ultralow thermal conductivity in diamond-type structures.

## Experimental Section

**Sample synthesis:** High purity Cu (shot, 99.99%), Ag (shot, 99.99%), Ga (shot, 99.999%), In (pellet, 99.999%) and Te (shot, 99.999%) were weighed and mixed according to the nominal compositions of $CuGaTe_2$, $AgGaTe_2$ and $CuInTe_2$. The stoichiometric mixtures (5 g for every sample) were sealed in evacuated quartz tubes (inner diameter of 10 mm and wall thickness of 1.5 mm) and slowly heated to 1323 K with the heating rate of 100 K $h^{-1}$ and held at this temperature for 24 h. Subsequently, the tubes were rapidly quenched in cool water to room temperature. The samples were then heated to 673 K at a rate of 100 K $h^{-1}$, annealed under vacuum at this temperature for 72 h and then slowly cooled to room temperature. The obtained ingots were crushed, hand ground into fine powder, and sintered by spark plasma sintering (SPS) at 773−823 K under a pressure of 40 MPa in a vacuum for 5 min to obtain densified samples.

**Characterization:** The room temperature phase structures of SPSed samples were examined by powder X-ray diffraction analysis (XRD; Rigaku Miniflex, Cu Kα)

**Synchrotron X-ray atomic pair distribution function (PDF) measurements:** Temperature dependent X-ray total scattering data were collected at 28-ID-1 beamline of the National Synchrotron Light Source II (NSLS II) at Brookhaven National Laboratory (referred to here and in the Main Text as experiment 1 or *exp 1*) and at P21.1 beamline of Positron-Elektron Tandem Ring Anlage (PETRA III) at Deutsches Elektronen Synchrotron (DESY) in Hamburg (experiment 2 or *exp 2*). Finely ground powders of $AgGaTe_2$ and $CuGaTe_2$ were sealed in 1.5 mm (outer diameter) quartz capillaries within a glovebox under light vacuum (*exp 1*) and under argon flow providing inert atmosphere (*exp 2*), and flame sealed. Measurements at NSLS II were carried out in capillary transmission geometry using a 2D PerkinElmer amorphous silicon area detector (2048 × 2048 pixels with 200 $\mu m^2$ pixel size) placed ~204 mm downstream of the sample. The setup utilized a monochromatic X-ray beam with 74.5 keV energy ($\lambda$ = 0.1665 Å). Sample temperature control was achieved using a FMB Oxford Hot Air Blower model GSB1300. Data for each sample were collected in 320 K – 485 K range in 5 K steps using 5 K/minute temperature ramp and 2 minutes thermalization at each temperature. Diffraction patterns at PETRA III were collected in a transmission geometry with an X-ray energy of 101.6 keV ($\lambda$ = 0.1221 Å) also using equivalent 2D PerkinElmer detector placed 432 mm behind the sample. The

sealed quartz capillaries were mounted in a Linkam THMS 600 furnace backfilled with nitrogen. The furnace contains a silver heating element with a 1.5 mm hole for the capillary, and two kapton windows for the X-ray beam. Data for each sample were collected over a temperature range from 300 K – 700 K in 25 K steps at a ramp rate of 2 K/minute. Samples were allowed to thermalize for 5 minutes per temperature step.

**PDF data processing and analysis:** Calibrations of the experimental geometry, momentum transfer (Q) range, and detector orientation were carried out by utilizing nickel standard measurements performed under the same conditions. Appropriate masking of the beam-stop shadow, inactive and outlier pixels, and subsequent azimuthal integration of the 2D images to obtain 1D diffraction patterns of intensity versus Q data were done using pyFAI software package[57, 58]. Standardized corrections to the data for experimental effects to obtain the reduced total scattering structure function, F(Q), and the subsequent sine Fourier transforms to obtain experimental PDFs, G(r), with $Q_{max}$=27 Å$^{-1}$ (*exp 1*) and $Q_{max}$=22 Å$^{-1}$ (*exp 2*) were carried out using the PDFgetX3 program within the xPDFsuite software package[59]. The PDF analysis was carried out using the PDFgui[60] modeling platform.

**Transport property measurements:** The electrical conductivity and the Seebeck coefficient were measured using the ZEM-3 apparatus (Ulvac Riko, Inc.) from 300−850 K under a He atmosphere. The thermal conductivity was obtained from the relationship $\kappa = DC_p\rho$, where $D$ is the thermal diffusivity measured by the laser flash diffusivity system (LFA 457; Netzsch) in Ar atmosphere. The specific heat ($C_p$) was calculated by Dulong–Petit law, and the sample density ($\rho$) was calculated by measuring the mass and dimensions of the sample. The electronic thermal conductivity was calculated by the Wiedemann-Franz relation, and the lattice thermal conductivity was estimated by subtracting the electronic thermal conductivity from the measured total thermal conductivity. The low-temperature (2−300K) heat capacity of $AgGaTe_2$ was measured using the Physical Property Measurement System (PPMS-9: Quantum Design). The ultrasonic pulse-echo method was used to determine the longitudinal and transverse sound velocities of the samples.

**Theoretical calculations:** We performed the density functional theory (DFT) calculations by using the Vienna ab initio simulation package (VASP)[61] implemented with the projected augmented wave (PAW) method. The generalized gradient approximated

functional proposed by Perdew, Burke, and Ernzerhof (GGA–PBE)[62] was chosen for estimating the exchange-correlation energy. High cut-off energy of 500 eV was set for the plane-wave basis. We adopted all the crystal structures from experimental data as an initial guess and then fully relaxed them with an energy convergence criterion of $10^{-6}$ eV until Hellmann–Feynman forces on each atom are less than 0.01 eV/Å.

A series of displaced 2×2×2 supercell (64 atoms) configurations are generated by Phonopy[63] to calculate the phonon dispersions and atom-projected density of states of diamondoid compounds *via* the finite-displacement method (FDM). The harmonic interatomic force constants (IFCs) were subsequently computed to estimate the phonon-phonon scattering rates. Another set of 64-atom supercell configurations was constructed by the code thirdorder.py[64] to generate the anharmonic IFCs for considering three-phonon scattering rates. We set a cut-off radius of 5 nm for atomic interactions to balance the accuracy and efficiency during the anharmonic IFC calculation. Any atomic interactions beyond this distance were not considered. Finally, the harmonic and anharmonic IFCs were used to calculate the single-mode parameters, *i.e.*, scattering rates, group velocities, and Gruneisen parameters, and solve the Peierls–Boltzmann transport equation iteratively with shengBTE code[64]. When calculating the $\kappa_L$, we used a dense 11×11×11 $q$-grid for Brillouin zone integration.

We note that because the directions of the Ag local distortions are random on the short-range, the DFT calculations cannot simulate this actual local behavior. However, the Ag local distortions would promote a global macroscopic distortion of the crystal structure which is reflected in large distortion parameter $\eta$. Thus, in this calculation, the local distortion effect is already included in the distorted crystal structure of $AgGaTe_2$ (the large crystallographic distortion parameter $\eta$).

## Supporting Information

Supporting Information is available from the Wiley Online Library or from the author.


## Acknowledgments

This work was primarily supported by a grant from the U.S. Department of Energy, Office of Science, and Office of Basic Energy Sciences under Award Number DE-SC0014520.

Work at Brookhaven National Laboratory was supported by U.S. Department of Energy, Office of Science, Office of Basic Energy Sciences (DOE-BES) under Contract No. DE-SC0012704. The X-ray PDF measurements were conducted in part on beamline 28-ID-1 of the National Synchrotron Light Source II, a U.S. Department of Energy (DOE) Office of Science User Facility operated for the DOE Office of Science by Brookhaven National Laboratory under Contract No. DE-SC0012704. We also acknowledge DESY (Hamburg, Germany), a member of the Helmholtz Association HGF, for the provision of experimental facilities. Parts of this research were carried out PETRA III, beamline P21.1.

## Author contributions

H.X. performed the sample synthesis, structural characterization, sound velocity measurement, and thermoelectric transport property measurements. E.B., M.A. and S.B. performed the synchrotron X-ray atomic pair distribution function (PDF) analysis. Z.L. and C.W. carried out the density functional theory calculations. All of the authors analyzed the data and discussed the underlying physics. H.X., E.B. and M.G.K. wrote the paper with contributions from the other authors. The manuscript reflects the contributions of all authors.

## Competing interests

The authors declare no competing interests.

## References

[1] K. Biswas, J. He, I. D. Blum, C. I. Wu, T. P. Hogan, D. N. Seidman, V. P. Dravid, M. G. Kanatzidis, *Nature* **2012**, *489*, 414.

[2] J. P. Heremans, V. Jovovic, E. S. Toberer, A. Saramat, K. Kurosaki, A. Charoenphakdee, S. Yamanaka, G. J. Snyder, *Science* **2008**, *321*, 554.

[3] Y. Pei, X. Shi, A. LaLonde, H. Wang, L. Chen, G. J. Snyder, *Nature* **2011**, *473*, 66.

[4] L. D. Zhao, S. H. Lo, Y. Zhang, H. Sun, G. Tan, C. Uher, C. Wolverton, V. P. Dravid, M. G. Kanatzidis, *Nature* **2014**, *508*, 373.

[5] L.-D. Zhao, G. Tan, S. Hao, J. He, Y. Pei, H. Chi, H. Wang, S. Gong, H. Xu, V. P. Dravid, C. Uher, G. J. Snyder, C. Wolverton, M. G. Kanatzidis, *Science* **2016**, *351*, 141.

[6] W. He, D. Wang, H. Wu, Y. Xiao, Y. Zhang, D. He, Y. Feng, Y.-J. Hao, J.-F. Dong, R. Chetty, L. Hao, D. Chen, J. Qin, Q. Yang, X. Li, J.-M. Song, Y. Zhu, W. Xu, C. Niu, X. Li, G. Wang, C. Liu, M. Ohta,

S. J. Pennycook, J. He, J.-F. Li, L.-D. Zhao, *Science* **2019**, *365*, 1418.
[7] B. Poudel, Q. Hao, Y. Ma, Y. Lan, A. Minnich, B. Yu, X. Yan, D. Wang, A. Muto, D. Vashaee, X. Chen, J. Liu, M. S. Dresselhaus, G. Chen, Z. Ren, *Science* **2008**, *320*, 634.
[8] C. Fu, S. Bai, Y. Liu, Y. Tang, L. Chen, X. Zhao, T. Zhu, *Nat. Commun.* **2015**, *6*, 8144.
[9] Y. Luo, J. Yang, Q. Jiang, W. Li, D. Zhang, Z. Zhou, Y. Cheng, Y. Ren, X. He, *Adv. Energy Mater.* **2016**, *6*, 1600007.
[10] H. Xie, X. Su, X. Zhang, S. Hao, T. P. Bailey, C. C. Stoumpos, A. P. Douvalis, X. Hu, C. Wolverton, V. P. Dravid, C. Uher, X. Tang, M. G. Kanatzidis, *J. Am. Chem. Soc.* **2019**, *141*, 10905.
[11] T. Plirdpring, K. Kurosaki, A. Kosuga, T. Day, S. Firdosy, V. Ravi, G. J. Snyder, A. Harnwunggmoung, T. Sugahara, Y. Ohishi, H. Muta, S. Yamanaka, *Adv Mater* **2012**, *24*, 3622.
[12] R. Liu, L. Xi, H. Liu, X. Shi, W. Zhang, L. Chen, *Chem. Commun.* **2012**, *48*, 3818.
[13] J. Zhang, R. Liu, N. Cheng, Y. Zhang, J. Yang, C. Uher, X. Shi, L. Chen, W. Zhang, *Adv Mater* **2014**, *26*, 3848.
[14] H. Xie, X. Su, G. Zheng, T. Zhu, K. Yin, Y. Yan, C. Uher, M. G. Kanatzidis, X. Tang, *Adv. Energy Mater.* **2016**, *7*, 1601299.
[15] H. Azimi, Y. Hou, C. J. Brabec, *Energy Environ. Sci.* **2014**, *7*, 1829.
[16] M. C. Ohmer, R. Pandey, *MRS Bulletin* **1998**, *23*, 16.
[17] H. Xie, S. Hao, S. Cai, T. P. Bailey, C. Uher, C. Wolverton, V. P. Dravid, M. G. Kanatzidis, *Energy Environ. Sci.* **2020**, *13*, 3693.
[18] H. Xie, S. Hao, T. P. Bailey, S. Cai, Y. Zhang, T. J. Slade, G. J. Snyder, V. P. Dravid, C. Uher, C. Wolverton, M. G. Kanatzidis, *J. Am. Chem. Soc.* **2021**, *143*, 5978.
[19] J. Zhang, L. Huang, C. Zhu, C. Zhou, B. Jabar, J. Li, X. Zhu, L. Wang, C. Song, H. Xin, D. Li, X. Qin, *Adv Mater* **2019**, *31*, e1905210.
[20] Y. Cao, X. Su, F. Meng, T. P. Bailey, J. Zhao, H. Xie, J. He, C. Uher, X. Tang, *Adv. Funct. Mater.* **2020**, *30*, 2005861.
[21] X. Su, N. Zhao, S. Hao, C. C. Stoumpos, M. Liu, H. Chen, H. Xie, Q. Zhang, C. Wolverton, X. Tang, M. G. Kanatzidis, *Adv. Funct. Mater.* **2018**, *29*, 1806534.
[22] Y. Zhu, B. Wei, J. Liu, N. Z. Koocher, Y. Li, L. Hu, W. He, G. Deng, W. Xu, X. Wang, J. M. Rondinelli, L.-D. Zhao, G. J. Snyder, J. Hong, *Mater. Today Phys.* **2021**, *19*. 100428.
[23] R. W. Keyes, *Phys. Rev.* **1959**, *115*, 564.
[24] I. V. Bodnar, L. V. Yasyukevich, *Tech. Phys.***2005**, *50*, 1178.
[25] R. L. Aggarwal, T. Y. Fan, *Appl. Opt.* **2005**, *44*, 2673.
[26] C. Rincón, M. L. Valeri-Gil, S. M. Wasim, *Phys. Status Solidi A* **1995**, *147*, 409.
[27] J. D. Beasley, *Appl. Opt.* **1994**, *33*, 1000.
[28] L. A. Makovetskaya, I. V. Bodnar, B. V. Korzun, G. P. Yaroshevich, *Phys. Status Solidi A* **1982**, *74*, K59.
[29] A. H. A. El Ela, N. Abdelmohsen, H. H. A. Labib, *Phys. Status Solidi A* **1982**, *71*, K219.
[30] A. H. A. el Ela, H. H. A. Labib, N. Abdelmohsen, *Phys. Status Solidi A* **1981**, *67*, K43.
[31] S. M. Wasim, *Phys. Status Solidi A* **1979**, *51*, K35.
[32] A. Miglio, C. P. Heinrich, W. Tremel, G. Hautier, W. G. Zeier, *Adv. Sci.* **2017**, *4*, 1700080.
[33] E. S. Božin, C. D. Malliakas, P. Souvatzis, T. Proffen, N. A. Spaldin, M. G. Kanatzidis, S. J. L. Billinge, *Science* **2010**, *330*, 1660.
[34] M. Dutta, K. Pal, M. Etter, U. V. Waghmare, K. Biswas, *J. Am. Chem. Soc.* **2021**, *143*, 16839.
[35] K. R. Knox, E. S. Bozin, C. D. Malliakas, M. G. Kanatzidis, S. J. L. Billinge, *Phys. Rev. B* **2014**, *89*. 014102.
[36] D. H. Fabini, G. Laurita, J. S. Bechtel, C. C. Stoumpos, H. A. Evans, A. G. Kontos, Y. S. Raptis, P. Falaras, A. Van der Ven, M. G. Kanatzidis, R. Seshadri, *J. Am. Chem. Soc.* **2016**, *138*, 11820.

[37] M. Dutta, M. V. D. Prasad, J. Pandey, A. Soni, U. V. Waghmare, K. Biswas, *Angew. Chem., Int. Ed.* **2022**, e202200071.
[38] T. Egami, S. J. Billinge, *Underneath the Bragg peaks: structural analysis of complex materials*, Elsevier, 2003.
[39] S. J. L. Billinge, I. Levin, *Science* **2007**, *316*, 561.
[40] G. Bocelli, G. Calestani, O. de Melo, F. Leccabue, C. Pelosi, B. E. Watts, *J. Cryst. Growth* **1991**, *113*, 663.
[41] R. Fouret, P. Derollez, A. Laamyem, B. Hennion, J. Gonzalez, *J. Phys.: Condens. Matter* **1997**, *9*, 6579.
[42] H. Xie, S. Hao, J. Bao, T. J. Slade, G. J. Snyder, C. Wolverton, M. G. Kanatzidis, *J. Am. Chem. Soc.* **2020**, *142*, 9553.
[43] P. Ying, X. Li, Y. Wang, J. Yang, C. Fu, W. Zhang, X. Zhao, T. Zhu, *Adv. Funct. Mater.* **2016**, *27*, 1604145.
[44] M. K. Jana, K. Pal, A. Warankar, P. Mandal, U. V. Waghmare, K. Biswas, *J. Am. Chem. Soc.* **2017**, *139*, 4350.
[45] H. Liu, J. Yang, X. Shi, S. A. Danilkin, D. Yu, C. Wang, W. Zhang, L. Chen, *J. Materiomics* **2016**, *2*, 187.
[46] N. Xu, M. Wyart, A. J. Liu, S. R. Nagel, *Phys. Rev. Lett.* **2007**, *98*, 175502.
[47] V. Lubchenko, P. G. Wolynes, *Proc. Natl. Acad. Sci.* **2003**, *100*, 1515.
[48] J. Callaway, H. C. von Baeyer, *Phys. Rev.* **1960**, *120*, 1149.
[49] J. Callaway, *Phys. Rev.* **1959**, *113*, 1046.
[50] X. L. Shi, X. Tao, J. Zou, Z. G. Chen, *Adv. Sci.* **2020**, *7*, 1902923.
[51] Z. Chen, X. Zhang, Y. Pei, *Adv Mater* **2018**, *30*, e1705617.
[52] M. N. Wybourne, B. J. Kiff, *J. Phys. C: Solid State Phys.* **1985**, *18*, 309.
[53] S. Kotochigova, Z. H. Levine, E. L. Shirley, M. D. Stiles, C. W. Clark. (2003), Atomic Reference Data for Electronic Structure Calculations (version 1.3). [Online] Available: http://physics.nist.gov/DFTdata. National Institute of Standards and Technology, Gaithersburg, MD. [54] G. Frenking, N. Fröhlich, *Chem. Rev.* **2000**, *100*, 717.
[55] C. R. Landis, T. K. Firman, D. M. Root, T. Cleveland, *J. Am. Chem. Soc.* **1998**, *120*, 1842.
[56] N. C. Pyper, *Philos. Trans. R. Soc., A* **2020**, *378*, 20190305.
[57] G. Ashiotis, A. Deschildre, Z. Nawaz, J. P. Wright, D. Karkoulis, F. E. Picca, J. Kieffer, *J. Appl. Crystallogr.* **2015**, *48*, 510.
[58] J. Kieffer, V. Valls, N. Blanc, C. Hennig, *J. Synchrotron Radiat.* **2020**, *27*, 558.
[59] P. Juhas, T. Davis, C. L. Farrow, S. J. L. Billinge, *J. Appl. Crystallogr.* **2013**, *46*, 560.
[60] C. L. Farrow, P. Juhas, J. W. Liu, D. Bryndin, E. S. Božin, J. Bloch, T. Proffen, S. J. L. Billinge, *J. Phys.: Condens. Matter* **2007**, *19*, 335219.
[61] G. Kresse, J. Furthmüller, *Phys. Rev. B* **1996**, *54*, 11169.
[62] J. P. Perdew, K. Burke, M. Ernzerhof, *Phys. Rev. Lett.* **1996**, *77*, 3865.
[63] A. Togo, I. Tanaka, *Scr. Mater.***2015**, *108*, 1.
[64] W. Li, J. Carrete, N. A. Katcho, N. Mingo, *Comput. Phys. Commun.* **2014**, *185*, 1747.

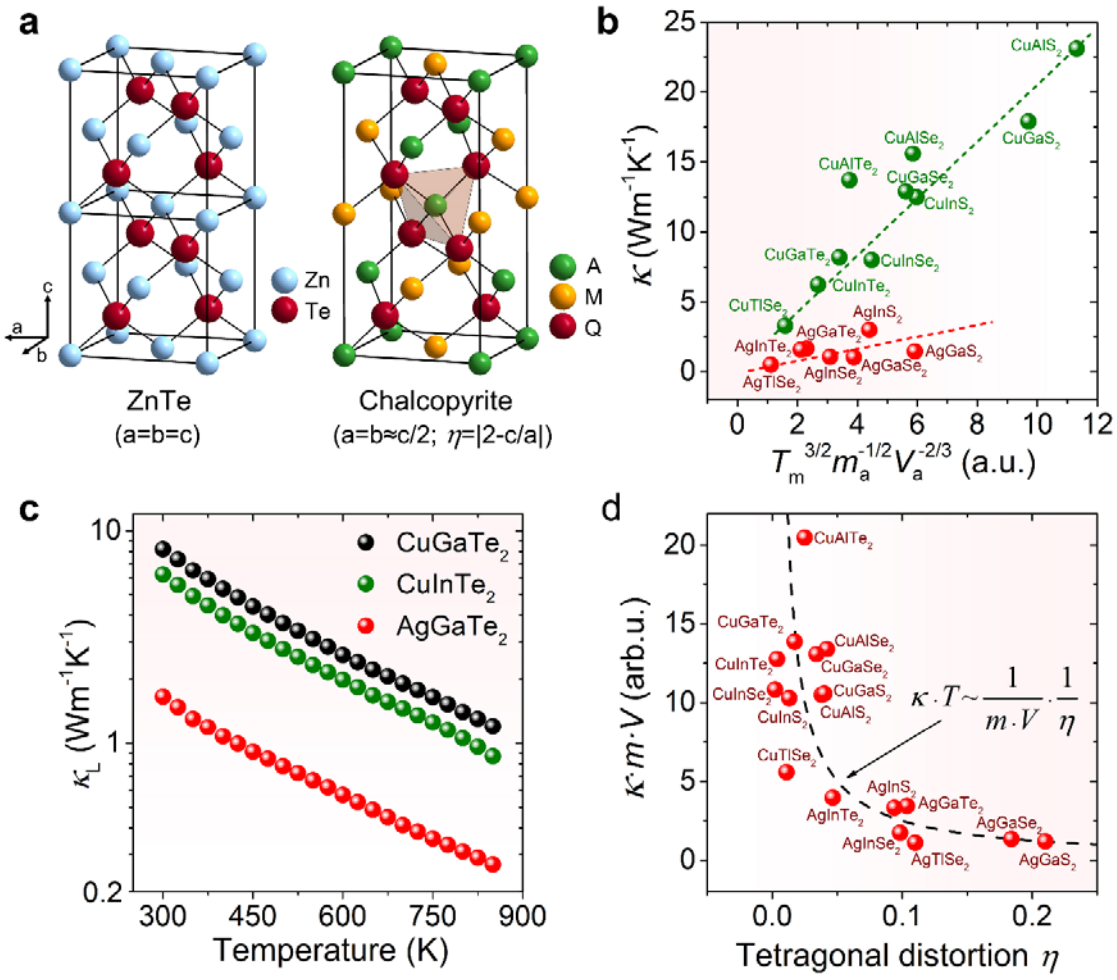


**Fig. 1. The thermal conductivities of diamondoid compounds are strongly related to the crystallographic distortion.** (**a**) Crystal structure of ZnTe and Chalcopyrite. (**b**) The room temperature thermal conductivities versus $T_m^{3/2} m_a^{-1/2} V_a^{-2/3}$ for different diamondoid compounds,[24-31] the dash line is a guide to the eye. (**c**) The temperature dependence of lattice thermal conductivity for $CuGaTe_2$ $CuInTe_2$ and $AgGaTe_2$. (**d**) The relationship between tetragonal distortion parameter ($\eta$ =|2-c/a|) and the thermal conductivity for different diamondoid compounds, the y-axis is the thermal conductivity multiplied by crystal volume ($V$) and formula weight ($m$), the dashed line shows the $1/\eta$ relationship.

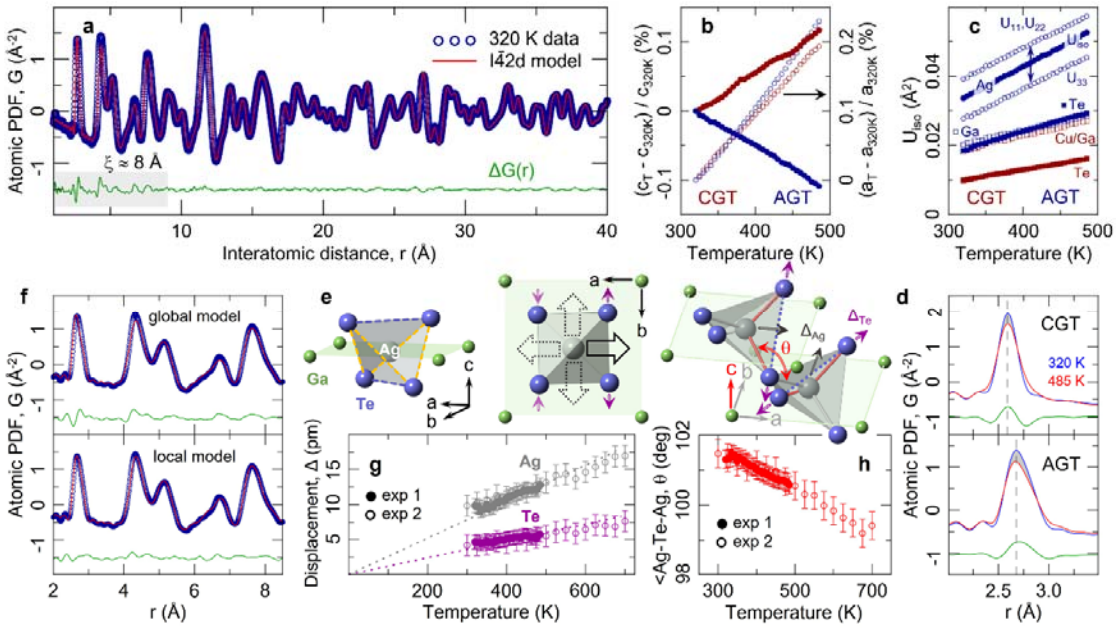


**Fig. 2. Local structure considerations in $AgGaTe_2$.** (**a**) Fit of crystallographic I$\bar{4}$2d model (red), describing global structure, to 320 K PDF data (blue). Their difference (green, offset for clarity) reveals discrepancy extending over a length-scale $\xi \approx 8$Å (gray region). (**b**) Relative change of $CuGaTe_2$ (CGT, red) and $AgGaTe_2$ (AGT, blue) tetragonal lattice parameters with temperature. The c-axis parameter of $AgGaTe_2$ exhibits negative thermal expansion. (**c**) Temperature dependence of atomic displacement parameters, $U_{iso}$, from the crystallographic model fits. The Ag and Te parameters for $AgGaTe_2$ are anomalously large compared to $CuGaTe_2$. (**d**) Comparison of the nearest neighbor PDF peak changes on warming in the two systems. The change in $AgGaTe_2$ is asymmetric with respect to the peak centroid (dashed line). (**e**) Local Ag environment (left), local distortion (middle), and coupling of local distortions on neighboring $AgTe_4$ tetrahedra (right). (**f**) Fit comparison of global (top) and local (bottom) models to short-range PDF data at 320 K. (**g**) Temperature evolution of Ag (gray) and Te (purple) local displacements extracted from distorted model. Dotted lines depict linear extrapolation to low temperature. (**h**) Temperature evolution of the Ag-Te-Ag angle θ in the distorted model defined in (**e**).

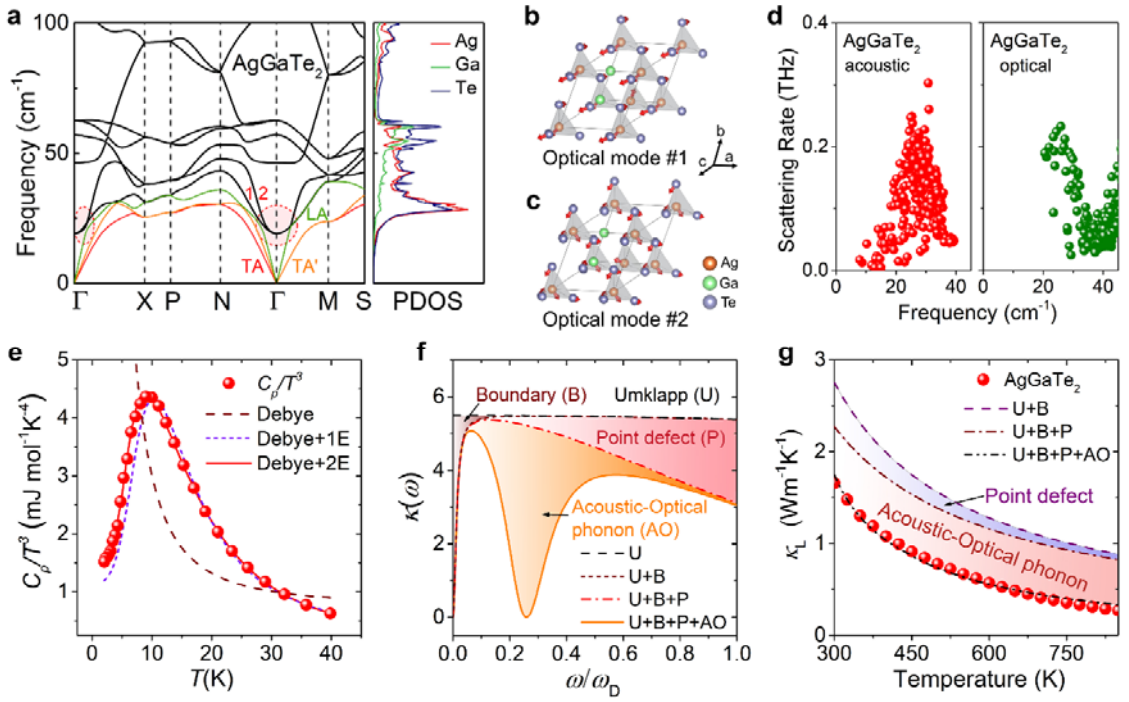


**Fig. 3. The strong acoustic-optical phonon scattering caused by local distortion of Ag is crucial to the low thermal conductivity of $AgGaTe_2$.** (**a**) DFT-calculated phonon dispersions and phonon density of states for $AgGaTe_2$, the pink regions showing a few extremely low frequency optical phonons emerge at the Γ point with a frequency of ~20 $cm^{-1}$. (**b**) and (**c**) The atomic vibrations in the primitive cell for the low frequency optical mode #1 and mode #2 of $AgGaTe_2$. (**d**) DFT-calculated phonon scattering rate for $AgGaTe_2$, the $AgGaTe_2$ exhibits unusually enhanced scattering rate at 20-35 $cm^{-1}$ for acoustic and optical phonons. (**e**) Low temperature heat capacity of $AgGaTe_2$ showing the relationship between $C_p/T^3$ and $T$. A peak is referred to Boson peak is observed and can be fitted with Debye+2Einstein model, implying the existence of acoustics-optical phonon coupling. (**f**) Calculated spectral lattice thermal conductivity $\kappa(\omega)$ for $AgGaTe_2$. (**g**) The lattice thermal conductivity of $AgGaTe_2$; the contribution of Umklapp scattering (U), grain boundary scattering (B), point defect scattering (P), and acoustic-optical phonon scattering (AO) were calculated by Debye-Callaway model.

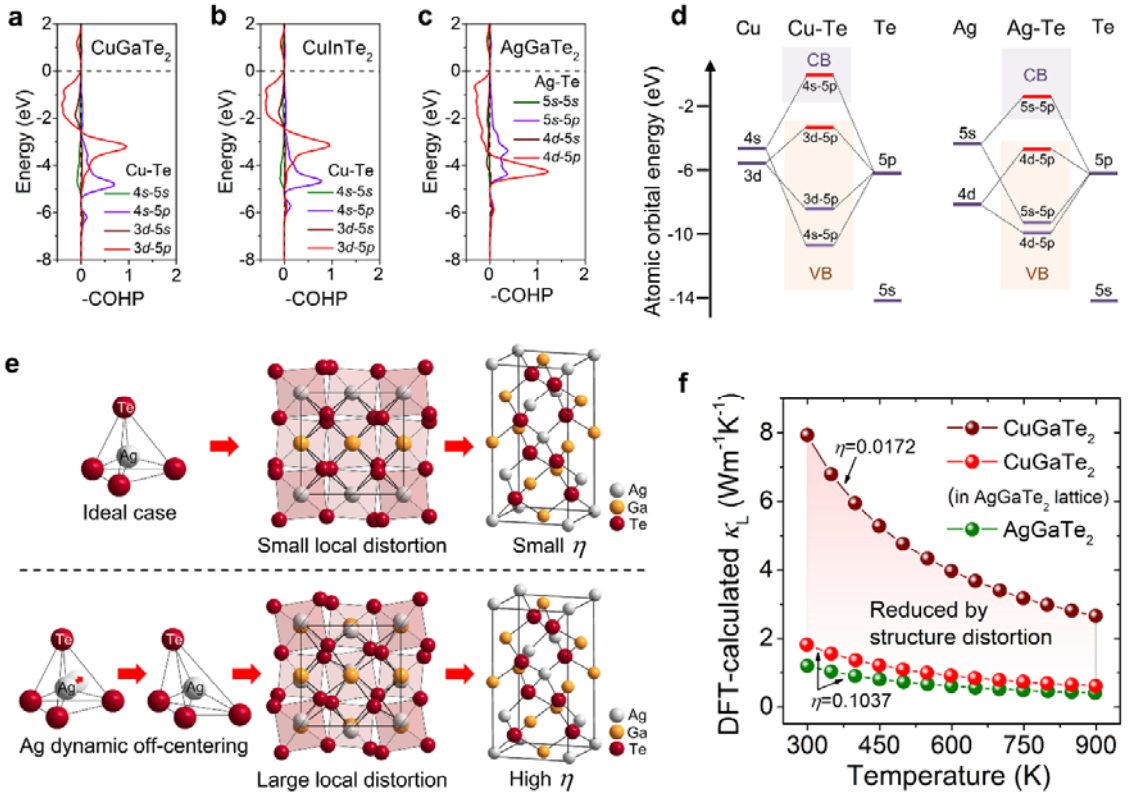


**Fig. 4. Dynamic off-centering of Ag leads to the large crystallographic distortion and low thermal conductivity.** The crystal orbital Hamiltonian populations (COHP) classified by different electronic orbital for (**a**) $CuGaTe_2$; (**b**) $CuInTe_2$ and (**c**) $AgGaTe_2$. (**d**) the schematic molecular orbital diagram of Cu-Te and Ag-Te bonding, the atomic orbital energy of Cu, Te and Ag are from NIST database LDA calculations.[53] The corresponding energy of bonding and anti-bonding states are deduced from the atomic orbital energy. (**e**) the schematic diagram illustrates the off-centering behavior of Ag leads to the large tetragonal distortion. (**f**) The DFT calculated thermal conductivities of $CuGaTe_2$, $AgGaTe_2$ and the hypothetical model that implants the ideal $CuGaTe_2$ ($\eta$ =0.0172) into the distorted $AgGaTe_2$ lattice ($\eta$ =0.1037). The predicted low thermal conductivity of this assumed structure (red points) implies the strong correlation between crystallographic distortion ($\eta$) and thermal conductivity in diamondoid structures.

**Table of contents**:

Weak $sd^3$ orbital hybridization of tetrahedral Ag atoms lead to the local symmetry breaking in the Ag-based diamondoid compounds. This local geometric distortion of Ag causes a global distortion of the crystal structure and results in the ultralow thermal conductivity. Based on this, the heat conductivity of diamondoid structure can be directly evaluated by the crystallographic distortion parameter.